The Astrophysical Journal, 904:54 (11pp), 2020 November 20 https://doi.org/10.3847/1538-4357/abbdfd

An Analysis of the North Polar Spur Using HaloSat

Daniel M. LaRocca[1], Philip Kaaret[1], K. D. Kuntz[2,3], Edmund Hodges-Kluck[2], Anna Zajczyk[1,2,4], Jesse Bluem[1], Rebecca Ringuette[1], and Keith M. Jahoda[2]

[1] University of Iowa, Department of Physics and Astronomy, Van Allen Hall, 30 N. Dubuque Street, Iowa City, IA 52242, USA; daniel-larocca@uiowa.edu
[2] NASA Goddard Space Flight Center, Greenbelt, MD 20771, USA
[3] The Henry A. Rowland Department of Physics and Astronomy, Johns Hopkins University, 3701 San Martin Drive, Baltimore, MD 21218, USA
[4] Center for Space Sciences and Technology, University of Maryland, Baltimore County, 1000 Hilltop Circle, Baltimore, MD 21250, USA
Received 2020 June 23; revised 2020 September 29; accepted 2020 October 2; published 2020 November 20

Abstract

We present HaloSat X-ray observations of the entirety of the bright X-ray emitting feature known as the North Polar Spur (NPS). The large field of view of HaloSat enabled coverage of the entire bright NPS in only 14 fields, which were each observed for ≈30,000 s. We find that the NPS fields are distinct in both brightness and spectral shape from the surrounding halo fields. We fit the NPS as two thermal components in ionization equilibrium with temperatures $kT_{\rm cool} \approx 0.087\ keV$ and $kT_{\rm hot} \approx 0.28\ keV$. We note a temperature gradient in the NPS hot component with an inner arc temperature warmer than the outer arc. The emission measures we find for the cool component of the NPS is a factor of 3–5 greater than that of the hot component, which suggests that the bulk of the NPS material is in the ≈0.1 keV component. We evaluate distance estimates of 0.4 and 8.0 kpc for the NPS. Our findings suggest a preference for a distant NPS with an energy of $\approx 6 \times 10^{54}$ erg, an age of ≈ 10 Myr, and pressures consistent with a 10μG magnetic field associated with the Fermi bubbles. The electron density $\approx 10 \times 10^{-3}\ {\rm cm}^{-3}$ is consistent with estimates for the shock region surrounding a Galactic-scale event.

Unified Astronomy Thesaurus concepts: X-ray astronomy (1810); Interstellar medium (847); Diffuse x-ray background (384); Superbubbles (1656)

1. Scientific Background

The ROSAT All-Sky Survey (RASS) shows prominent features in the 3/4 keV map in the vicinity of the Galactic center (Snowden et al. 1995). One such feature appears on the X-ray sky as a 15° wide arc extending from near the Galactic plane at Galactic coordinates $l \approx 27°$, $b \approx 10°$, up toward the north Galactic pole at around $l \approx 330°$, $b \approx 78°$ commonly referred to as the North Polar Spur (NPS). This X-ray emission feature is due to large volumes of hot, ionized interstellar plasma, but the ultimate origin of this plasma remains poorly understood.

An area of strong synchrotron emission with a high fractional polarization known as Loop I is located in the direction of the NPS in the sky, possibly forming a boundary layer (Spoelstra 1973). Early astronomers postulated the NPS to be a shell of patchy emission arising from a nearby supernova remnant (SNR; Hanbury Brown et al. 1960). However, the velocity of the neutral gas surrounding the NPS suggests an age of 10^6 yr old, which would place the SNR beyond its radiative phase (Heiles et al. 1980). Egger & Aschenbach (1995) interpreted the NPS as the limb-brightened shell of a shock-heated local superbubble swept out by the supernova and stellar winds of the Scorpio–Centaurus OB association. The large size, the apparent asymmetry in the sky, and the high latitude extent of the NPS provide a compelling case for a local interpretation.

However, the work by Sofue has suggested that the NPS could be better understood as a shock front propagating through the Galactic halo. This shock would have originated at the Galactic center with an energy of 3×10^{56} erg around 15 million years ago (Sofue et al. 1974; Sofue 2000). The source of the energy would be a starburst or some explosive event resulting in a dumbell-shaped shock front or bipolar hypershells.

Several recent studies provide support for a more distant interpretation of the NPS. The most prominent is the discovery of large regions of gamma-ray emission near the Galactic center known as the Fermi bubbles (FBs) using the Fermi-LAT data (Su et al. 2010). The NPS traces the outer arc of the FB suggesting that the NPS could be a region of Galactic halo material compressed by the FB (Su et al. 2010). Puspitarini et al. (2014) compared 3D maps of the interstellar dust distribution to the ROSAT X-ray background map to search for a possible local cavity that might serve as a source of NPS emission and found that their results do not support the existence of such a cavity. Lallement et al. (2016) observed the low latitude extent of the NPS and claimed that it is absorption bounded rather than emission bounded. They place a lower boundary of at least 260 pc on the NPS, but favor a distance as far as 4 kpc.

Kataoka et al. (2013) examined a series of Suzaku fields and suggested that the NPS is well described by a weak shock driven by the Fermi bubble expansion with $v_{\rm exp} \approx 300\ {\rm km\ s^{-1}}$, which is compressing the Galactic halo to form a $kT \approx 0.3$ keV feature seen as the NPS. Akita et al. (2018) conducted an analysis of 16 Suzaku fields in the NPS ranging from mid- to high latitudes and found that the emission measures (EMs) of the NPS component implied a minimum path length through the NPS of 0.9 kpc, which is in stark contrast with the dimensions suggested for a local object. They describe a two-step explosion scenario where the NPS is the result of the first explosion 15–25 Myr ago releasing 10^{56-57} erg into a structurally asymmetric Galactic halo. The following explosion 5–10 Myr ago could have resulted in the largely symmetric Fermi bubbles seen, as the first explosion had blown away most of the halo gas (Akita et al. 2018).

Table 1
NPS Pointings and Coordinates

Target Name	R.A.[a] (°)	Decl.[b] (°)	l[c] (°)	b[d] (°)	Exposure[e] (ks)	GTI[f] (ks)
HS0025	267.0	3.0	28.30	15.47	43.9	11.7
HS0026	260.5	8.0	29.94	23.50	59.3	46.2
HS0027	255.0	3.0	22.27	26.05	58.1	44.4
HS0028	251.0	12.0	29.46	33.66	117.7	88.1
HS0029	246.0	5.0	19.19	34.86	113.6	93.8
HS0030	241.0	14.0	26.62	43.36	35.0	26.8
HS0031	236.5	7.5	15.79	44.27	138.1	41.7
HS0032	230.5	14.0	20.09	52.57	91.5	62.9
HS0033	222.0	11.5	8.89	58.50	127.8	102.0
HS0034	223.0	20.0	24.95	61.55	85.3	53.1
HS0035	215.0	19.0	15.84	68.11	117.8	86.5
HS0036	212.0	11.0	354.76	65.83	94.7	65.9
HS0037	206.0	16.5	354.50	73.84	125.4	71.1
HS0038	201.0	10.0	328.61	71.23	148.9	96.7

Notes.
[a] R.A. of HaloSat pointing center in J2000.
[b] Decl. of HaloSat pointing center in J2000 equinox.
[c] Galactic longitude of HaloSat pointing center.
[d] Galactic latitude of HaloSat pointing center.
[e] Sum of exposure time for the three HaloSat detectors.
[f] Good time interval seconds remaining after cuts.

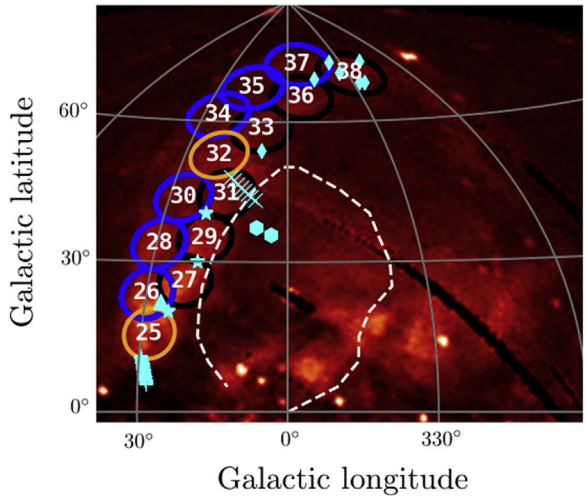

Figure 1. The HaloSat NPS pointings in Galactic coordinates on the ROSAT 3/4 keV image. The fields are annotated by their HaloSat IDs, circles indicate the full-response fields of view for each pointing, and colors designate the outer arc (blue), the inner arc (black), and the ridge (orange). Other fields examined previously are also denoted by cyan markers. The Suzaku fields: those analyzed by Miller et al. (2008) (triangle), by Ursino et al. (2015) (hexagons), Kataoka et al. (2013) (eight crosses) and Akita et al. (2018) (thin diamond). The XMM-Newton fields: those analyzed by Willingale et al. (2003) (three stars), and by Lallement et al. (2016) (19 pluses). The northern Fermi bubble coordinates from Su et al. (2010) are shown as a white dashed line.

2. HaloSat Observations of the NPS

HaloSat is an instrument optimized for observations of diffuse X-ray emitting structures (Kaaret et al. 2019; LaRocca et al. 2020). It has a large field of view, the spectra are moderately well resolved, and the CubeSat nature provides the flexibility to schedule observations to reduce sources of foreground contamination. HaloSat carries three X-ray silicon drift detectors sensitive in the 0.4–7.0 keV energy band with average energy resolutions of 84.9 eV at the 676 eV F Kα line and 137.4 eV at the 5.9 keV Mn Kα line, comparable to XMM-Newton and Suzaku (Kaaret et al. 2019). The HaloSat full-response field of view is a 10° diameter circle, which makes it a useful tool to probe X-ray emission from diffuse structures such as the NPS.

We conducted HaloSat observations of the NPS in 2019 and 2020 with a total exposure of 462 ks. These observations adhered to the HaloSat strategies for minimizing contamination of solar wind charge exchange (Kuntz 2019). These observations consisted of 14 distinct pointing directions for roughly 30 ks each. A summary of exposures, field directions, and filtered exposure times are given in Table 1. The locations of these fields with respect to the ROSAT 3/4 keV map are shown in Figure 1. This image also shows existing XMM-Newton and Suzaku observations of the NPS analyzed in other referenced work. In addition, the outline of the northern Fermi bubble, as described in Su et al. (2010), is depicted.

Unfiltered event files were generated for each observation containing all events recorded while the detectors were operating nominally using standard HaloSat screening criteria. The event files were filtered to remove periods of elevated particle background contamination by applying cuts to the rates of events in the "HARD" band (3.0–7.0 keV) and the "VLE" band (>7.0 keV). Filtering based on the HARD count rate was set at an upper limit of 0.16 counts s^{-1} on 64 s time bins, and the upper limit of 0.60 counts s^{-1} was placed on the VLE band. The resulting good time interval times can be seen in Table 1. X-ray energies were calculated from event pulse heights using temperature-dependent calibration coefficients (A. Zajczyk et al. 2020, in preparation).

3. Spectral Model

All spectral modeling and fitting were completed simultaneously for the three HaloSat detectors using XSPEC (v12.10.1f; Arnaud 1996). The standard response matrices used in the analysis were generated via detector simulation with parameters tuned to match ground calibration data obtained over a range of temperatures (Zajczyk et al. 2018). Fitting could be conducted for HaloSat spectra for energies between 0.4–7.0 keV. The 3.0–7.0 keV energy band was used to fit the background and the 0.4–3.0 keV band was used to fit the astrophysical model components.

The spectral model for the NPS fields includes emission components for the local hot bubble (LHB), the cosmic X-ray background (CXB), and the NPS. The total model used is "apec + TBabs*(power) + TBabs*(vapec + vapec)" corresponding to the LHB, the CXB, and the cool and hot NPS. A separate "pegpwrlw" component for the instrumental background was used with a diagonal response. The best-fit models of representative spectra can be seen in Figure 2. All errors are reported with 90% confidence intervals.

3.1. The Local Hot Bubble

A local unabsorbed thermal plasma is known to dominate X-ray observations near 0.25 keV (Snowden et al. 1990). The source of this emission has been deemed the LHB. Several lines of observational evidence has demonstrated that emission from the LHB originates within the Local Cavity, a region remarkably devoid of neutral material (Knapp 1975). The Local Cavity is not necessarily filled with warm gas, and instead forms a boundary beyond which the observed softer LHB emission would not penetrate. The boundaries of the emission

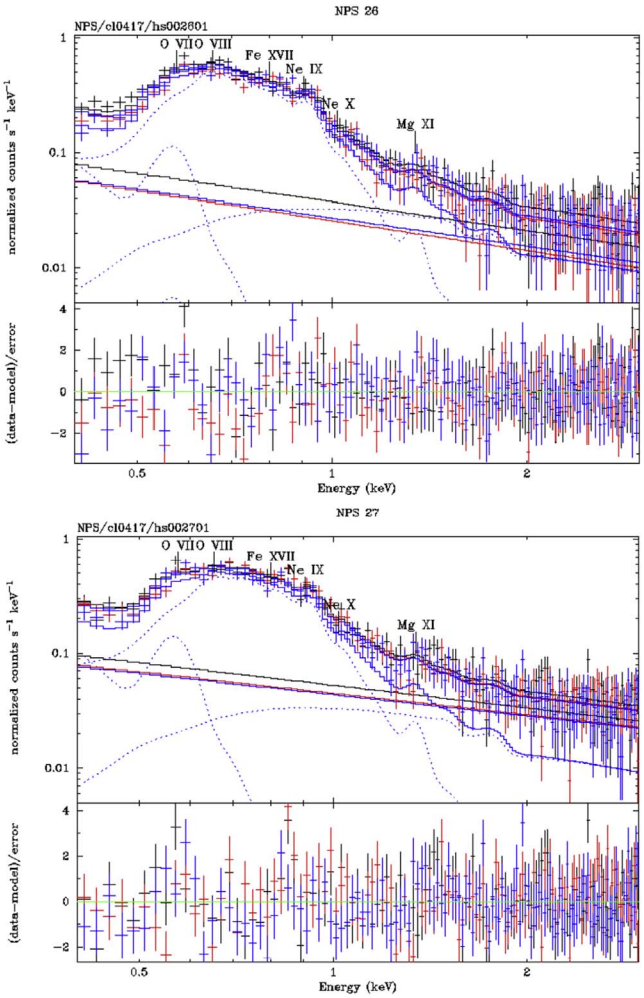

Figure 2. Spectra from two representative HaloSat fields modeled by an NPS with two thermal components, absorbing column density fixed at a fraction of 0.6 of $n_{\rm H,Gal}$, and the kT of the cool NPS component fixed at the weighted average of 0.087 keV. The data points correspond to the three HaloSat detectors. The three lines are associated with the induced particle background power law with normalization values specific for each detector. The absorbed power-law component is associated with the cosmic X-ray background. The NPS hot thermal component dominates most emission below 1 keV, and the NPS cool thermal component shows prominent emission below 0.7 keV.

region track the location of a sharp increase in neutral column density reasonably well (Lallement 2004).

A recent study used the DXL sounding rocket measurements to characterize the LHB. They found it to be well modeled by an unabsorbed thermal plasma and generated maps of the EM and temperature with an average temperature of 0.097 ± 0.013 keV (Liu et al. 2016). The LHB is expected to be isothermal and thus a single temperature was adopted for all fields (Liu et al. 2016). We adopt a HaloSat response-weighted average of the Liu et al. (2016) mapped EM values for each of the individual fields.

For this analysis, the LHB was modeled as an unabsorbed apec model. The kT of this apec model was frozen at 0.1 keV for all NPS fields. The normalization of this apec was frozen for each field at the value associated with the response-weighted average emission measure for the field taken from Liu et al. (2016), though we discuss the examination of a bright LHB commonly seen in the literature in Section 4.1. It should be noted that these values fall within an extrapolated region and may be less reliable; however, the contribution of the LHB should have a negligible impact on the fit parameters of the other components.

3.2. Absorption

All interstellar absorption was modeled with the TBabs model (Wilms et al. 2000). Understanding the total Galactic X-ray column in a given direction allows us to place an upper bound on expected X-ray absorbing columns for Galactic objects. The best-fit X-ray absorbing column for an emission source is commonly compared to the total Galactic X-ray absorbing column as a tracer of distance in the Galaxy.

For the total Galactic X-ray column density, it is common to adopt a value from the measurements of total Galactic neutral hydrogen column measurements. We expect the H I column density to underestimate the Galactic X-ray absorbing column density, particularly for fields with H I column densities greater than $\approx 3 \times 10^{20}$ cm^{-2}, high enough to expect molecular clouds in the line of sight.

Instead, dust maps can serve as a tracer of heavier elements that contribute more to X-ray absorption in the relevant energy band. To estimate the Galactic absorbing column density along a line of sight, we use the Planck satellite maps of optical extinction based on the dust radiance with point sources removed (Collaboration et al. 2014; Green 2018). We adopt the conversion coefficient of 2.47×10^{21} H cm^{-2} mag^{-1} (Zhu et al. 2017).

With the large field of view of HaloSat, the values of $E(B-V)$, and thus our converted $n_{\rm H,Gal}$, vary across the region. A simple average of $n_{\rm H,Gal}$ for a field is not appropriate. Instead, we use the TBabs cross sections to calculate the absorption curves for all values of $n_{\rm H,Gal}$ from a grid of points within the field of view. We then fit the response-weighted average of the absorption curves to determine an equivalent total $n_{\rm H,Gal}$.

3.3. The Cosmic X-Ray Background

The contribution to the CXB from unresolved extragalactic point sources is commonly modeled as a power law subjected to absorption with full Galactic absorbing column density. A recent study of the CXB using Chandra modeled the CXB with no removal of X-ray sources, which more directly corresponds to nonimaging satellites such as HaloSat (Cappelluti et al. 2017). Their fit yielded an absorbed power law with a photon index of 1.45 ± 0.02 and a normalization of 10.91 ± 0.16 photons cm^{-2} s^{-1} sr^{-1} keV^{-1} (Cappelluti et al. 2017). We fix the photon index to 1.45. Using the HaloSat response-weighted effective field-of-view solid angle of 0.0350 sr (Kaaret et al. 2019); their normalization was converted to a normalization of 0.38 photons keV^{-1} cm^{-2} s^{-1} for the HaloSat FOV in spectral analysis and was fixed. The X-ray absorption was modeled using TBabs.

3.4. Instrumental Background

The instrumental background was modeled as a power law with photon index calculated from the hard band (3.0–7.0 keV) count rate. This component was not folded through an auxiliary response file, and the redistribution matrix was diagonal. The normalization values were determined by modeling the fixed CXB described above and fitting for the instrumental background components for each individual field in the 3.0–7.0 keV

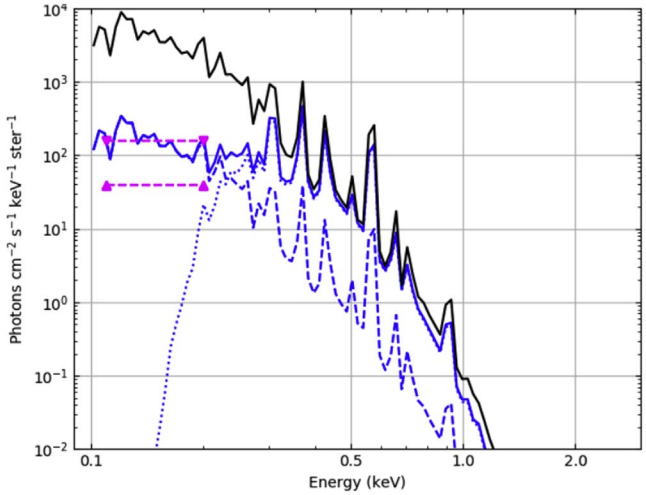

Figure 3. An intrinsic model comparison of a bright LHB (solid black) vs. a dim LHB (dashed blue) + bright cool NPS component (dotted blue) for a representative field extrapolated down to the ROSAT R1 energy band 0.11–0.2 keV. The upper and lower bounds of the ROSAT R1 count rates for the HaloSat fields are the dashed magenta lines.

band. The best-fit normalization values for the induced particle background component were fixed in further analysis.

4. X-Ray Spectra of the North Polar Spur

4.1. NPS Spectral Model

Spectral descriptions of the NPS are often modeled using two components with different temperatures, and therefore emission from the NPS is often modeled as the sum of two optically thin thermal plasmas: a cooler component with $kT \approx 0.1$ keV and a hot component with $kT \approx 0.3$ keV (Willingale et al. 2003; Miller et al. 2008; Kataoka et al. 2013; Akita et al. 2018). While the hot component is always associated with the NPS, the interpretation of the cool component varies depending on the study and has been associated with the LHB, the Galactic halo, and the NPS.

4.1.1. The LHB as the Cool Component

The cool component used in Kataoka et al. (2013) and Akita et al. (2018) is interpreted as the LHB, and is thus unabsorbed. Notably, in both studies the spectral fitting has a low-energy cutoff of 0.4 keV and the authors do not examine the low-energy implications of their spectral model.

We have attempted to fit our spectra using either an absorbed or an unabsorbed cool component. With a low-energy cutoff for HaloSat of 0.4 keV, both models were successful. We extrapolated our best-fit models down to 0.1 keV and compared to the RASS R1 count rates for our fields with results shown in Figure 3. The unabsorbed cool component (solid black line) significantly overestimates the RASS R1 count rates (lower and upper bounds are indicated with dashed magenta lines), while the absorbed cool component (dotted blue line) does not contribute substantially in the R1 energy band. The addition of the LHB component (dashed blue line) described in Section 3.1 alone is sufficient to account for the count rates seen at low energies; thus, any additional components must be subjected to enough absorption to minimally impact this energy band. We conclude that the cool plasma is not local and should be subjected to interstellar absorption.

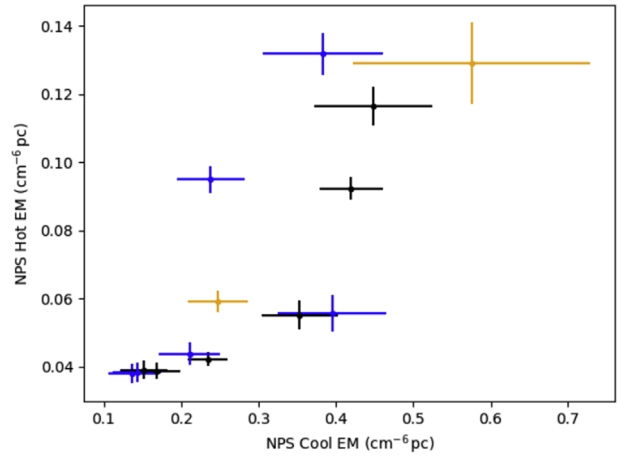

Figure 4. An examination of the emission measures (EMs) for the cool and hot components of the 14 NPS fields indicates a physical association between the two components. Colors designate the outer arc (blue), the inner arc (black), and the ridge (orange).

4.1.2. The Halo as the Cool Component

The cool component may also be associated with the Galactic halo of the Milky Way. In the event that the cool component is associated with the halo it would be subjected to interstellar absorption. Willingale et al. (2003) and Miller et al. (2008) both interpret the cool component as a Galactic halo subjected to full Galactic interstellar absorption. The spectral fitting procedure used by Willingale et al. (2003) includes a simultaneous fit of the XMM-Newton data with the RASS 0.1–0.4 keV. The Miller et al. (2008) spectral fitting includes the Suzaku Back-Illuminated X-ray Imaging Spectrometer with a low-energy cutoff of 0.3 keV. Both of these studies include a component associated with the LHB consistent with the EM values seen in Liu et al. (2016).

If the component were to be associated with the halo, the path length through the cool NPS X-ray emitting plasma would likely be different than for the hot NPS component and would impact our physical interpretation of the results. We compared the NPS cool component to measurements for the halo from HaloSat fields in the southern Galactic hemisphere and found the EM values of the NPS cool component to be consistently larger by a factor of 5–10 (Kaaret et al. 2020). The EM of the cool component in the NPS fields is also much higher than the EM seen in adjacent HaloSat fields, which suggests that the cool component is not primarily associated with the Galactic halo.

If the cool component were due to only the halo, then its emission measure in the direction of the NPS should be similar to that observed outside of the NPS. However, the cool component in the direction of the NPS is much stronger for all NPS fields than the local halo fields.

4.1.3. The NPS as the Cool Component

As the cool component can be due to neither the LHB nor the Galactic halo, it must be due predominantly to the NPS. This conclusion is supported by the correlation of the strength of the cool component with the strength of the hot NPS component as seen in Figure 4. Given the similar temperatures of the cool NPS component and the Galactic halo, we can do no more to separate the two. Furthermore, the variation in the strength of the Galactic halo reported by Kaaret et al. (2020)

suggests that interpolation of the halo emission to the location of the NPS would be insufficient.

The cool component will include some unknown amount of halo emission, but will be dominated by the NPS emission. The fields that are enhanced in NPS hot EM compared to NPS cool EM are 25–29, the lowest latitude and brightest fields of the NPS. We adopt the interpretation that the cool component has a physical association with the NPS.

4.2. Spectral Fitting

We model the NPS as two optically thin thermal plasmas in ionization equilibrium (vapec) subjected to the same interstellar absorption. We model our NPS components with an elemental abundance of 0.3 of the solar value except for 0.45 for Ne. The Ne enrichment was required to successfully remove the persistent residuals near the 0.91 keV Ne IX emission feature.

The distance to the NPS is a source of contentious debate and greatly impacts any physical interpretation of the object. The X-ray absorbing column density can be used as a tracer of distance as the amount of X-ray absorbing material in front of an object increases with the object's distance increases along a given line of sight. However, the majority of the X-ray absorbing material is confined to regions relatively close to the plane of the Galaxy. Therefore, the absorbing column for an object distance of 500 pc may be consistent with full Galactic absorption. This is well illustrated by Figure 11 of Lallement et al. (2016). Our spectral analysis proved insensitive to fitting absorbing column density in a manner that would assist with making substantive claims on a distance to the NPS.

Our absorption fitting yielded inconsistent results from field to field. Similar to other reported results (Kataoka et al. 2013; Ursino et al. 2015; Akita et al. 2018), we found that without placing upper bounds our best-fit absorbing column densities were larger than the determined full Galactic column for 10 of 14 fields. For X-ray absorption, we fixed our column densities at a value of 0.6 of the Galactic absorption for that field. This fraction was motivated by results reported in the literature adjusted for our method of determining Galactic absorbing column densities (Willingale et al. 2003; Miller et al. 2008; Lallement et al. 2016). This value fell within 90% confidence intervals of the best fit for 11 of 14 fields.

4.3. Best-fit Results

We fit the model of the NPS as described for temperatures and normalizations of both thermal components. The best-fit temperatures of the cool NPS component had a weighted average of 0.087 keV with $\chi^2/\mathrm{DoF} = 16.8/13$, which can be seen in Figure 5. In further analysis, we fixed the kT of the cool component to 0.087 keV.

The best-fit results of our model can be seen in Table 2 and Figure 6, with errors depicted by 90% confidence intervals. Figure 2 shows the fits to representative spectra. For the hot NPS component, we tested whether our results were consistent with a constant temperature. We found an average kT of 0.274 keV with a $\chi^2/\mathrm{Dof} = 90.6/13$, which suggests the temperature is not constant. Instead, there appears to be a gradient of temperatures, which are highest in the inner arc (black points) and lowest at the outer arc (blue points).

The EM values for both components decrease as the angle from the Galactic center increases, just as expected from examination of the ROSAT All-Sky maps.

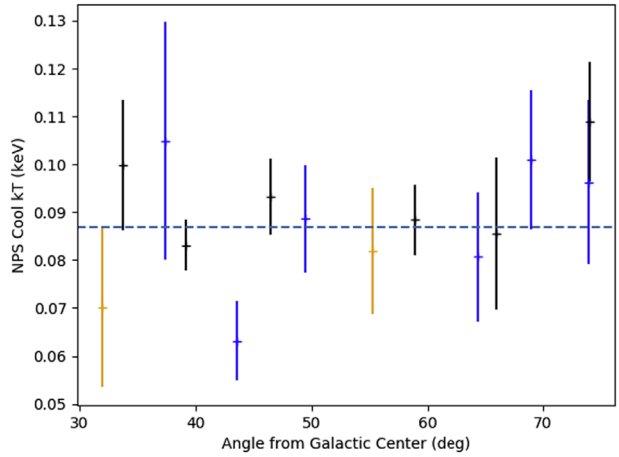

Figure 5. Best-fit NPS with a thawed cool NPS component kT. The weighted average kT was calculated to be 0.087 keV (dashed line), which was fixed in further analysis. Colors designate the outer arc (blue), the inner arc (black), and the ridge (orange).

5. Physical Properties of the North Polar Spur

The NPS is typically thought in terms of the component ≈0.3 keV. However, we have shown that the object is not quite that simple and includes emission from plasma at lower temperatures, which is commonly attributed to other sources. We can use our best-fit properties of the cool and hot NPS components to better understand the physical properties of the NPS and the physical nature of these two temperature components.

5.1. Distance and Physical Properties

It is necessary to know the distance and geometry of the NPS in order to translate the EM and kT values obtained by spectral fitting into physical parameters such as electron density and thermal energy. Determining the path length can give an idea of the object's size and some insight to the distance.

Following the procedure in Akita et al. (2018), we can estimate the range of path lengths $h \approx EM/{n_e}^2$ for the NPS hot component assuming constant electron densities. If there is no large variation in magnetic field between the LHB and a local interpretation of the NPS, Ursino et al. (2015) estimate $n_e = 1.6 \times 10^{-3}\,\mathrm{cm}^{-3}$, and thus we might expect NPS hot path lengths between 14.8 and 51.6 kpc. Adopting instead the upper bound of $n_e = 10 \times 10^{-3}\,\mathrm{cm}^{-3}$ from Sofue et al. (2016) for the shock region of the Galactic center hypershell, we might expect NPS hot path lengths between 0.4–1.3 kpc. These path lengths are inconsistent with a local object of the scale expected in the literature. However, a primary flaw in this approach stems from the lack of reliable estimates for the density either in the local interpretation or a distant Galactic-scale object.

We thus choose instead to examine two possibilities for the distance: 0.4 kpc and 8.0 kpc. Using these distances we can estimate the path length through the X-ray emitting gas by adopting the assumption that it is roughly symmetric about a central axis, and therefore its width on the sky would provide an estimate of the path length. The width of the NPS can be calculated as $2d\tan(\theta/2)$, where d is the distance and θ is the angular width of the NPS on the sky. We measure an angular width by determining a set of inner and outer arc boundary coordinates and measuring the minimum angular distance between the arcs at each of our points. To determine the

Table 2
Best-fit values for the Two Thermal Components of the NPS

HSID	$n_H/n_{H,Gal}$ [a]	kT_{hot} [b] (keV)	EM_{hot} [c] (10^{-2} cm^{-6} pc)	kT_{cool} [d] (keV)	EM_{cool} [e] (10^{-2} cm^{-6} pc)	χ^2/dof
25	0.6	0.286 ± 0.012	12.9 ± 1.3	0.087	57.6 ± 15.8	460.4/384
26	0.6	0.267 ± 0.005	13.2 ± 0.6	0.087	38.3 ± 8.5	656.4/384
27	0.6	0.289 ± 0.008	11.7 ± 0.6	0.087	44.9 ± 7.7	526.9/384
28	0.6	0.254 ± 0.004	9.5 ± 0.4	0.087	23.8 ± 4.6	568.5/384
29	0.6	0.272 ± 0.004	9.2 ± 0.4	0.087	42.0 ± 4.4	577.4/384
30	0.6	0.277 ± 0.013	5.6 ± 0.6	0.087	39.5 ± 7.3	594.7/384
31	0.6	0.314 ± 0.014	5.5 ± 0.4	0.087	35.3 ± 5.5	466.2/384
32	0.6	0.280 ± 0.008	5.9 ± 0.3	0.087	24.8 ± 4.5	569.8/384
33	0.6	0.305 ± 0.009	4.2 ± 0.2	0.087	23.5 ± 2.6	498.8/384
34	0.6	0.252 ± 0.007	4.4 ± 0.4	0.087	21.1 ± 4.7	577.2/384
35	0.6	0.245 ± 0.008	3.8 ± 0.3	0.087	13.6 ± 3.1	426.4/384
36	0.6	0.312 ± 0.010	3.9 ± 0.3	0.087	15.2 ± 3.2	579.7/384
37	0.6	0.252 ± 0.009	3.8 ± 0.3	0.087	14.3 ± 3.6	477.8/384
38	0.6	0.283 ± 0.009	3.9 ± 0.3	0.087	16.9 ± 3.3	506.5/384

Notes.
[a] Fraction of nH used for TBabs NPS absorption.
[b] kT of the NPS hot absorbed vapec component.
[c] EM of the NPS hot absorbed vapec component.
[d] kT of the NPS cool absorbed vapec component.
[e] EM of the NPS cool absorbed vapec component.

boundary coordinates we examined ROSAT R45 count rates over a range of Galactic latitudes sweeping across the NPS using a 5° radius aperture. The boundaries were taken at our best estimate of the half-maximum of the count rates in the R45 peak. This procedure was successful for Galactic latitudes between 10° and 40°. Above 40° the boundaries were determined using the ROSAT R45 all-sky map.

We adopt an angular width of 17° for the NPS, which we determined by calculating the minimum angle between each outer arc coordinate and the inner arc coordinates. For the local interpretation we find a path length 0.12 kpc and for the distant interpretation we find a path length of 2.39 kpc. We adopt these distance and path length estimates for the purpose of physical interpretation.

Using the distance, path length, and best-fit values from our spectral analysis we can make a measurement of several physical properties of the two thermal components of the NPS. The electron density can be calculated using

$$n_e \approx \sqrt{EM/(h\,f)}\,, \tag{1}$$

where EM is the emission measure, f is the volume filling fraction, and h is the path length through the object along the line of sight. Thus, the electron density we measure is proportional to the distance and the volume filling factor:

$$n_e \;\propto\; d^{-1/2} f^{-1/2}. \tag{2}$$

We adopt a volume filling factor of 0.5 for both the hot and cool NPS thermal components. The pressure is

$$p \approx n_e\, kT. \tag{3}$$

Therefore, the pressure we measure is proportional to the electron density and is then proportional to the distance and the volume filling factor:

$$p \;\propto\; d^{-1/2} f^{-1/2}. \tag{4}$$

Energy can be calculated from

$$E \approx n_e\, kT\; V = n_e\, kT\; \Omega\, d^2\, h\, f, \tag{5}$$

where V the volume of the X-ray emitting gas in the line of sight and Ω is the response-weighted field of view of HaloSat, which is equal to 0.0350 sr. The energy we measure is then proportional to the distance and the volume filling factor:

$$E \;\propto\; d^{5/2} f^{1/2}. \tag{6}$$

The cooling timescale τ for the object to radiate away its energy at its current luminosity can then be taken as

$$\tau = \frac{E}{L}. \tag{7}$$

The intrinsic luminosities were calculated for the 0.0001–3.0 keV band. The results appear in Tables 3 and 4, and are plotted in Figure 7.

If the NPS is a limb-brightened shell of emitting material, the expected geometry would require line-of-sight path lengths to increase by a factor of ≈ 2–3, with the inner arc path lengths underestimated more than those of the outer arc. This would cause electron densities and pressures to decrease by a factor of $\approx \sqrt{2} - \sqrt{3}$ and stated energies and cooling timescales to increase by a factor of $\approx \sqrt{2} - \sqrt{3}$.

5.2. A Distant Interpretation

For a distance of 8.0 kpc, we find a total energy from all 14 fields to be $\approx 6 \times 10^{54}$ erg, with 2.3×10^{54} erg in the hot NPS component and 3.6×10^{54} erg in the cool NPS component. The energy required for an object at 8.0 kpc is consistent with several thousand supernova, if heated in situ, or some form of energy injection from the Galactic center. This energy might be consistent with a fraction of the energy estimate expected of a first explosion starburst activity or AGN-like outburst with an energy of 10^{56-57} erg (Kataoka et al. 2018).

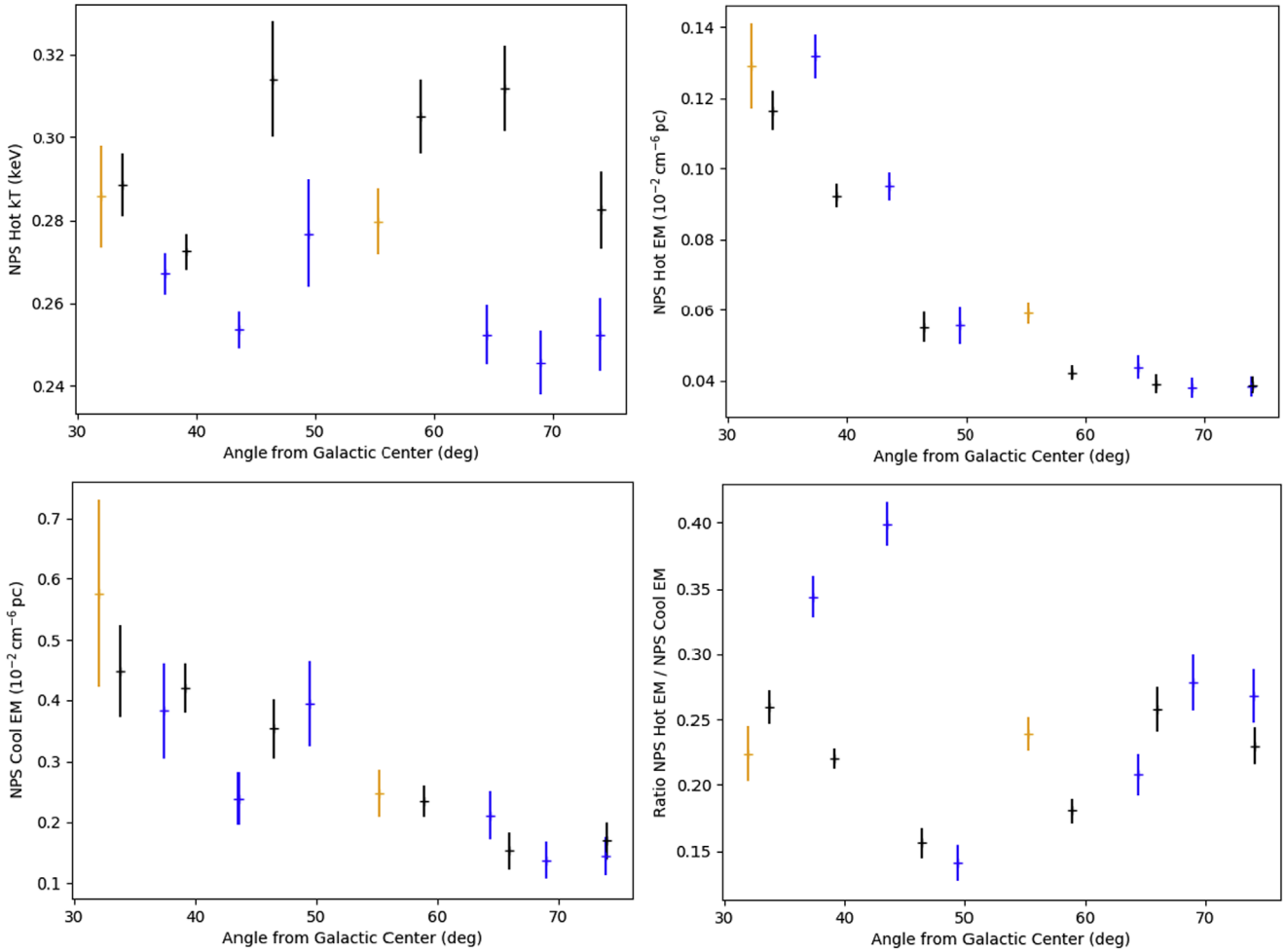

Figure 6. The best-fit results of the NPS modeled by two thermal components with absorbing column densities fixed to 0.6 $n_{\rm H,Gal}$ and the kT of the cooler component fixed to the weighted average of 0.087 keV. Color indicates the inner arc fields (black), the outer arc fields (blue), and the ridge fields (orange).

For a distant interpretation, we expect the electron density to be $\approx 10 \times 10^{-3}$ cm^{-3} in the shock front (Sofue et al. 2016). We find this electron density estimate to be consistent with the densities we measure for the NPS.

To examine the distant pressure measurement of $\approx$1–5 $\times 10^{-12}$ dyne cm^{-2}, we estimated the magnetic field for the environment and determined a magnetic pressure. A 10 μG magnetic field inferred in the Fermi bubbles by Su et al. (2010) would produce a magnetic pressure of 5.7×10^{-12} dyne cm^{-2}. This value is plotted as dashed blue lines in Figure 7. The magnetic field inferred from the Fermi bubbles is consistent with the pressures we measure for the NPS.

Additionally, we can estimate the age of the object based on the cooling timescale. These estimates serve as upper bounds because they assume energy is lost only via radiation and not through other means such as heating the surrounding gas. For the distant interpretation, we find an age estimate of $\approx$100 Myr for the hot component and $\approx$10 Myr for the cool component. This is fairly consistent with the posited starburst activity or AGN-like outburst 15–25 Myr ago, or the event 5–10 Myr ago believed to have created the Fermi bubbles (Akita et al. 2018).

Another estimate of age is based upon the time required for the object with a uniform expansion velocity to reach its current size or $\tau = r_s/v_s$, where r_s is the radial distance and v_s is the expansion velocity. From X-ray spectral analysis, Kataoka et al. (2013) find the expansion velocity to be 320 km s^{-1} from the ratio of temperatures $kT_1/kT_0 = 0.3$ keV/0.2 keV for the NPS expanding into the Galactic halo. Miller & Bregman (2016) find the expansion velocity of the Fermi bubbles through the halo to be 490 km s^{-1} from a ratio of temperatures $kT_1/kT_0 = 0.43$ keV/0.17 keV. We use an NPS temperature of 0.274 keV associated with the hot component, and if we assume the NPS is expanding into the halo, we can adopt a halo temperature of 0.2 keV from Kataoka et al. (2013) and $\gamma = 5/3$. We find a mach number $\approx$1.4, which yields an expansion velocity of 240 km s^{-1} for a 170 km s^{-1} sound speed. For a 4 kpc radial expansion distance, we determine an age of 16 Myr.

If instead the NPS was a strong shock propagating through the cold interstellar medium (ISM) we determine an expansion velocity of $\approx$470 km s^{-1}, which yields an age estimate of 8 Myr for a 4 kpc radial expansion distance. In either case, these age estimates are consistent with the expected age of the Fermi bubbles.

The hydrodynamic simulations of the Galactic center hypershell model by Sofue et al. (2016) predict a temperature increase at the shock front in the X-ray emitting gas with warmer temperatures on the inner arc and cooler temperatures on the outer arc. We find a temperature gradient that could be evidence of this prediction, though spectral analysis with higher spatial resolution observations across the NPS would be

Table 3
Physical Parameters for an NPS at a Distance 8.0 kpc, a Path Length of 2.39 kpc, and a Filling Factor 0.5

HSID	n_{hot} [a]	p_{hot} [b]	E_{hot} [c]	τ_{hot} [d]	n_{cool} [e]	p_{cool} [f]	E_{cool} [g]	τ_{cool} [h]
25	10.4	4.8	3.74	1.09	22.0	3.1	2.41	0.06
26	10.5	4.5	3.53	0.96	17.9	2.5	1.96	0.07
27	9.9	4.6	3.59	1.17	19.4	2.7	2.13	0.06
28	8.9	3.6	2.85	1.02	14.1	2.0	1.55	0.09
29	8.8	3.8	3.02	1.19	18.7	2.6	2.06	0.07
30	6.8	3.0	2.38	1.58	18.2	2.5	1.99	0.07
31	6.8	3.4	2.69	1.93	17.2	2.4	1.89	0.07
32	7.0	3.2	2.48	1.56	14.4	2.0	1.58	0.09
33	5.9	2.9	2.29	2.12	14.0	2.0	1.54	0.09
34	6.1	2.4	1.93	1.49	13.3	1.9	1.46	0.09
35	5.6	2.2	1.75	1.51	10.7	1.5	1.17	0.11
36	5.7	2.9	2.25	2.27	11.3	1.6	1.24	0.11
37	5.7	2.3	1.80	1.59	10.9	1.5	1.20	0.11
38	5.7	2.6	2.03	1.96	11.9	1.7	1.30	0.10

Notes.
[a] Electron density of the hot NPS component (10^{-3} cm^{-3}).
[b] Pressure of the hot NPS component (10^{-12} dyne cm^{-2}).
[c] Energy of the hot NPS component (10^{53} erg).
[d] Cooling timescale of the hot NPS component (10^{2} Myr).
[e] Electron density of the cool NPS component (10^{-3} cm^{-3}).
[f] Pressure of the cool NPS component (10^{-12} dyne cm^{-2}).
[g] Energy of the cool NPS component (10^{53} erg).
[h] Cooling timescale of the cool NPS component (10^{2} Myr).

Table 4
Physical Parameters for an NPS at a Distance 0.4 kpc, a Path Length 0.12 kpc, and a Filling Factor of 0.5

HSID	n_{hot} [a]	p_{hot} [b]	E_{hot} [c]	τ_{hot} [d]	n_{cool} [e]	p_{cool} [f]	E_{cool} [g]	τ_{cool} [h]
25	46.5	21.3	2.09	0.24	98.2	13.7	1.35	0.01
26	46.9	20.1	1.98	0.21	80.1	11.2	1.10	0.02
27	44.1	20.4	2.01	0.26	86.6	12.1	1.19	0.01
28	39.9	16.2	1.59	0.23	63.1	8.8	0.87	0.02
29	39.3	17.1	1.69	0.27	83.8	11.7	1.15	0.01
30	30.5	13.5	1.33	0.35	81.3	11.3	1.11	0.02
31	30.4	15.3	1.50	0.43	76.9	10.7	1.05	0.02
32	31.4	14.1	1.39	0.35	64.4	9.0	0.88	0.02
33	26.6	13.0	1.28	0.47	62.6	8.7	0.86	0.02
34	27.1	10.9	1.08	0.33	59.4	8.3	0.81	0.02
35	25.2	9.9	0.98	0.34	47.7	6.7	0.65	0.03
36	25.6	12.8	1.26	0.51	50.4	7.0	0.69	0.02
37	25.3	10.2	1.01	0.36	48.9	6.8	0.67	0.03
38	25.5	11.5	1.13	0.44	53.1	7.4	0.73	0.02

Notes.
[a] Electron density of the hot NPS component (10^{-3} cm^{-3}).
[b] Pressure of the hot NPS component (10^{-12} dyne cm^{-2}).
[c] Energy of the hot NPS component (10^{50} erg).
[d] Cooling timescale of the hot NPS component (10^{2} Myr).
[e] Electron density of the cool NPS component (10^{-3} cm^{-3}).
[f] Pressure of the cool NPS component (10^{-12} dyne cm^{-2}).
[g] Energy of the cool NPS component (10^{50} erg).
[h] Cooling timescale of the cool NPS component (10^{2} Myr).

better suited for searching for the fine structure noted in the simulations.

5.3. A Local Interpretation

For a distance of 0.4 kpc we find the total energy from all 14 fields to be 3.3×10^{51} erg with 2.0×10^{51} erg in the hot NPS component and 1.3×10^{51} erg in the cool NPS component. This energy is consistent with several supernova with thermalization efficiency lower than 1, where the mechanical energy injected from the blast wave may not all be radiative.

A local NPS electron density is expected to be $n_e = 2.5 \times 10^{-3}$ cm^{-3} from Egger & Aschenbach (1995), which is an order of magnitude lower than we find in the local interpretation of the NPS.

To examine the local pressure measurement of $\approx$10–20 $\times 10^{-12}$ dyne cm^{-2}, we once again estimated the magnetic field for the environment and determined a magnetic pressure. The magnetic field for the local environment has been measured to be 2.1 μG (Ferriere 2001), which would produce a magnetic pressure of 3.9×10^{-14} dyne cm^{-2}. The measurement of pressure we find for a local interpretation is significantly higher than the magnetic field expected in the local ISM. Even for a larger estimate of the magnetic field of 4.9 μG adopted by Ursino et al. (2015), the local interpretation is still inconsistent.

For the local interpretation, we find an age estimate based on the cooling timescale of $\approx$30 Myr for the hot component and $\approx$2 Myr for the cool component, which is significantly larger than predicted estimates of 0.2 Myr (Egger & Aschenbach 1995).

5.4. An Emission-measure Distribution

Thus far, we have interpreted the NPS in view of the two temperature components that we have measured. A two-temperature model frequently provides a good description of the X-ray spectrum from hot gas in supernova remnants and galaxies, at least at modest energy resolution. By observing face-on galaxies where there may be multiple discrete emission regions per resolution element, Kuntz & Snowden (2010) demonstrated that these temperatures are merely loci for a range of more complex temperature distributions. That is, the best-fit temperatures may not be physically meaningful.

To investigate what we can learn from these temperatures, we assume that the true temperature distribution is continuous and can be parameterized through the differential emission measure (DEM), which defines the amount of gas emitting at each temperature. An analytical model for the DEM that may be appropriate for the NPS is described in Gayley (2014). This model, which is appropriate for either a cooling flow or shock-heated gas, describes gas that is heated to some initial temperature and then cools in pressure equilibrium. This model is of interest for two reasons: it was motivated by and accounts for the frequently measured ratio of $\sim$3 between the hot and cool temperatures in two-temperature models, and the NPS morphology suggests an expanding blast wave.

However, the cooling model is not consistent with our results because such a model must have a DEM that increases with temperature. In pressure equilibrium, the density of cooling gas must increase as the temperature decreases, which further increases the cooling rate (in the regime of interest where line cooling is strong). Thus, cooling starts slowly and then accelerates, meaning that in the X-ray band the emission measure is dominated by hotter gas. In the NPS, we find a significantly higher cool emission measure.

It is possible, but unlikely, that the large cool emission measure is consistent with the Gayley (2014) model due to the limited signal and energy resolution of the data. We simulated models in XSPEC in which gas cools from an initial

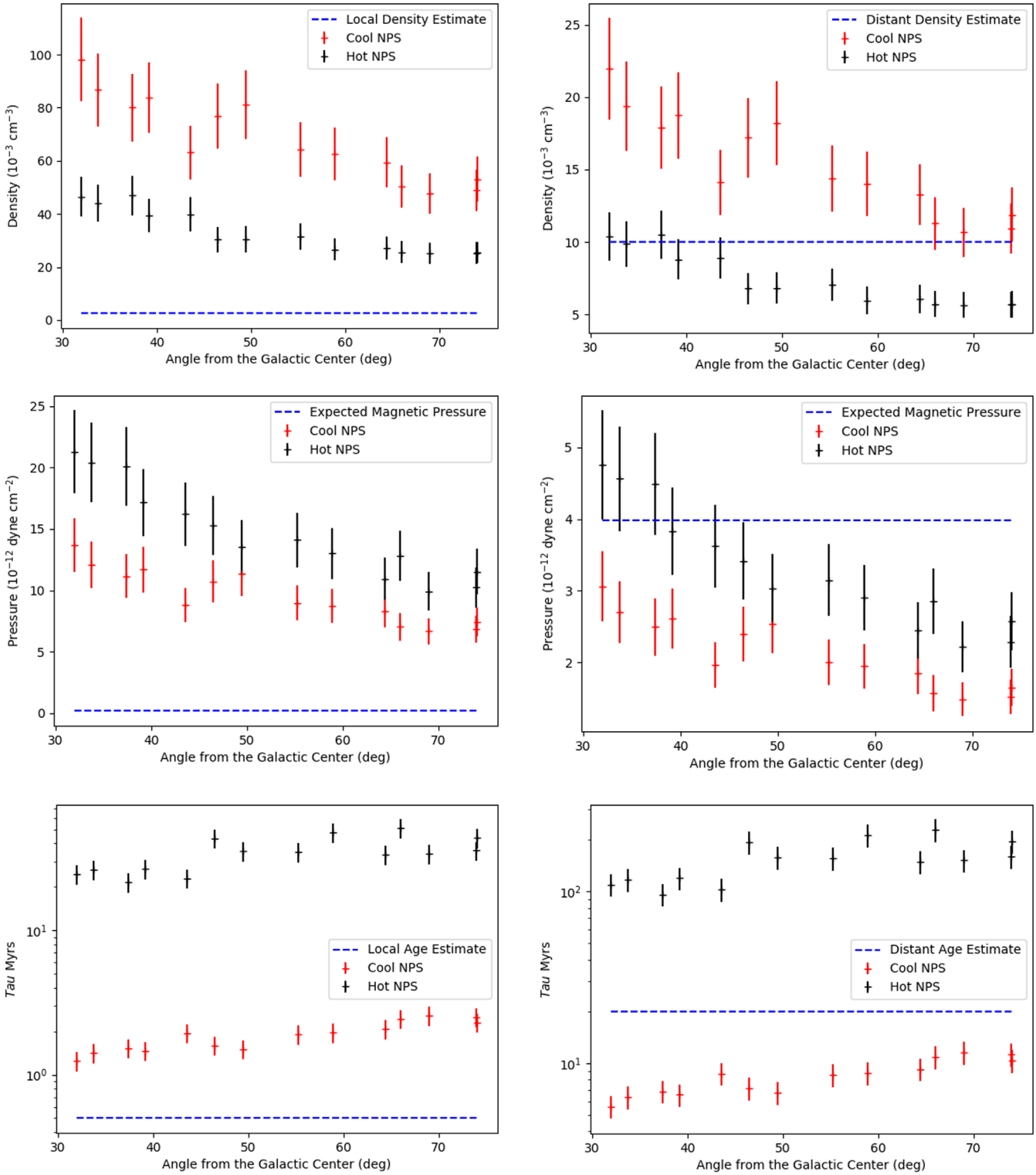

Figure 7. The physical properties of the 0.4 kpc (left) and 8.0 kpc (right) distance assumptions. Expected values based on the distance are depicted as blue dashed horizontal lines, which correspond to the local electron density estimate of 2.5×10^{-3} cm^{-3} (Egger & Aschenbach 1995), the distant electron density estimate of 10×10^{-3} cm^{-3} (Sofue et al. 2016), the expected magnetic pressure from a 2.1 μG local magnetic field (Ferriere 2001), a 10 μG distant magnetic field associated with the Fermi bubbles (Su et al. 2010), the local age estimate of 0.1 Myr (Egger & Aschenbach 1995), and the 20 Myr age estimate of the Fermi bubbles (Akita et al. 2018). Error bars depict the uncertainty due to an increase or decrease of 30% in the distance assumption.

$kT = 0.2$–0.4 keV using the HaloSat response, the same absorption column, and a similar data quality, and we found that it is possible to adequately fit the data using models with a cool temperature near 0.1 keV and a hot temperature near 0.3 keV, with up to 95% of the emission measure in the cool component. This can occur because the 0.3 keV component produces much more line emission than the 0.1 keV component and because the 0.1 keV component is largely absorbed. However, these models are not typically the *best* fit, and these simulations indicate that it would be unlikely to find a

consistently high emission-measure ratio between the cool and hot components, whereas we report a large ratio in most NPS fields.

We therefore conclude that the DEM is dominated by cooler gas, which implies that the morphology traced by the 3/4 keV ROSAT map does not represent the bulk of the material. Such a DEM cannot be explained by cooling from a single, initial temperature in the steady state, but there are a few possible explanations. First, the NPS may represent shock-heated material with a range of initial densities (i.e., a shock wave propagating into a fractal or clumpy interstellar or halo medium). The downstream temperature depends primarily on the shock velocity, but subsequent cooling will be faster in the denser regions, which can contain a large fraction of the mass. Second, the cool-dominant DEM could be produced by a range of shock speeds, as in a complex and multiphase wind. If most gas experiences weaker shocks, it will be heated to lower initial temperatures. Third, the DEM may be an artifact of superposition with the cool gas and hot gas not causally connected at all.

These possibilities can be summarized as cooling in shocked gas, cooling in shocked gas with a range of upstream densities, and cooling in shocked gas with a spectrum of shock velocities. They are not mutually exclusive. Despite the different phenomenology of the DEM in the Gayley (2014) and the other cases, the shock needed to produce them is not much different. If the DEM maps to cooling of shocked material with an initial $kT = 0.2$–0.4 keV, the shock must propagate at a few hundred km s^{-1}, whereas the short cooling time of denser, X-ray emitting gas below $kT = 0.2$ keV implied by the emission-measure ratio in our fits is consistent with the projected width of the NPS in the distant interpretation for this speed. The required shock velocities are also consistent with inferences of the velocity of material in the Fermi bubbles for the distant interpretation (Miller & Bregman 2016; Ashley et al. 2020).

In summary, the remaining ambiguity in how our best-fit model maps to the true emission-measure distribution does not prevent us from using the cool-dominant scenario described above to draw conclusions about the origin of the NPS.

6. Conclusion

Using the soft X-ray spectrometer on board the HaloSat CubeSat, we took the first moderately resolved observations of the entire bright emission feature of the NPS. We fit the NPS as two thermal components in ionization equilibrium. We find a hot component associated with 3–4 MK gas and a cool component associated with 1 MK gas. We note a temperature gradient in the NPS hot component with an inner arc temperature warmer than the outer arc.

We find that the interpretation of the cooler ($kT \approx 0.1$ keV) thermal emission component in the region of the NPS as due to the LHB is inconsistent with ROSAT data in the 0.11–0.2 keV energy band. The emission measure of the cooler fitted component is 3–5 times greater than that of the hotter component, suggesting that, while the $\approx$0.3 keV component is prominent for the NPS, the bulk of the material present is in the $\approx$0.1 keV component.

We estimate the physical parameters of the X-ray emitting plasma for two different distances corresponding to interpretations of the NPS as a Galactic-scale outflow versus a superbubble-scale event. Our findings suggest a preference for a distant NPS. The energy $\approx 6 \times 10^{54}$ erg and estimated age of 10 Myr are reasonable for a two-explosion origin of the NPS. The pressures we find are consistent with a 10 μG magnetic field associated with the Fermi bubbles. The electron density $\approx 20 \times 10^{-3}$ cm^{-3} is consistent with estimates for the shock region surrounding a Galactic-scale event.

This research was supported by NASA grant No. NNX15AU57G. This research was also supported by the NASA Iowa Space Grant under award No. NNX16AL88H. We acknowledge Steven Spangler, Cornelia Lang, and Casey DeRoo for their useful comments discussions that helped to improve the work. We acknowledge our support from NASA GSFC particularly the work of Thomas Johnson, the hard work of all the individuals at the University of Iowa that helped make HaloSat a success, the Blue Canyon Technologies team for their work on the spacecraft bus and for acting as the mission operation center, and the WFF UHF Ground Station Team for their support of HaloSat in orbit. We acknowledge the contribution from our anonymous reviewer, whose comments helped to clarify the presentation of this work.

Software: XSPEC (v12.10.1f; Arnaud 1996), dustmaps (Green 2018).

ORCID iDs

Daniel M. LaRocca https://orcid.org/0000-0002-7529-4619
Philip Kaaret https://orcid.org/0000-0002-3638-0637
K. D. Kuntz https://orcid.org/0000-0001-6654-5378
Edmund Hodges-Kluck https://orcid.org/0000-0002-2397-206X
Jesse Bluem https://orcid.org/0000-0001-8307-7166
Rebecca Ringuette https://orcid.org/0000-0003-0875-2023

References

Akita, M., Kataoka, J., Arimoto, M., et al. 2018, ApJ, 862, 88
Arnaud, K. 1996, in ASP Conf. Ser. 101, Astronomical Data Analysis Software and Systems V, ed. G. H. Jacoby & J. Barnes (San Francisco, CA: ASP), 17
Ashley, T., Fox, A. J., Jenkins, E. B., et al. 2020, ApJ, 898, 128
Cappelluti, N., Li, Y., Ricarte, A., et al. 2017, ApJ, 837, 19
Collaboration, P., Ade, P., Aghanim, N., et al. 2014, A&A, 571, A16
Egger, R. J., & Aschenbach, B. 1995, A&A, 294, L25
Ferriere, K. M. 2001, RvMP, 73, 1031
Gayley, K. G. 2014, ApJ, 788, 90
Green, G. M. 2018, JOSS, 3, 695
Hanbury Brown, R., Davies, R., & Hazard, C. 1960, Obs, 80, 191
Heiles, C., Chu, Y.-H., Troland, T., Reynolds, R., & Yegingil, I. 1980, ApJ, 242, 533
Kaaret, P., Zajczyk, A., LaRocca, D., et al. 2019, ApJ, 884, 162
Kaaret, P., Koutroumpa, D., Kuntz, K. D., et al. 2020, NatAs, 4, 1072
Kataoka, J., Sofue, Y., Inoue, Y., et al. 2018, Galax, 6, 27
Kataoka, J., Tahara, M., Totani, T., et al. 2013, ApJ, 779, 57
Knapp, G. 1975, AJ, 80, 111
Kuntz, K. 2019, A&ARv, 27, 1
Kuntz, K., & Snowden, S. 2010, ApJS, 188, 46
Lallement, R. 2004, A&A, 418, 143
Lallement, R., Snowden, S., Kuntz, K. D., et al. 2016, A&A, 595, A131
LaRocca, D. M., Kaaret, P., Kirchner, D. L., et al. 2020, JATIS, 6, 014003
Liu, W., Chiao, M., Collier, M. R., et al. 2016, ApJ, 834, 33
Miller, E. D., Tsunemi, H., Bautz, M. W., et al. 2008, PASJ, 60, S95
Miller, M. J., & Bregman, J. N. 2016, ApJ, 829, 9
Puspitarini, L., Lallement, R., Vergely, J.-L., & Snowden, S. 2014, A&A, 566, A13
Snowden, S., Cox, D., McCammon, D., & Sanders, W. 1990, ApJ, 354, 211
Snowden, S. L., Freyberg, M., Plucinsky, P., et al. 1995, ApJ, 454, 643
Sofue, Y. 2000, ApJ, 540, 224
Sofue, Y., Habe, A., Kataoka, J., et al. 2016, MNRAS, 459, 108
Sofue, Y., Hamajima, K., & Fujimoto, M. 1974, PASJ, 26, 399

Spoelstra, T. 1973, A&A, 24, 149
Su, M., Slatyer, T. R., & Finkbeiner, D. P. 2010, ApJ, 724, 1044
Ursino, E., Galeazzi, M., & Liu, W. 2015, ApJ, 816, 33
Willingale, R., Hands, A., Warwick, R., Snowden, S., & Burrows, D. N. 2003, MNRAS, 343, 995
Wilms, J., Allen, A., & McCray, R. 2000, ApJ, 542, 914
Zajczyk, A., Kaaret, P., Kirchner, D., et al. 2018, Proc. AIAA/USU Conf. on Small Satellites, Upcoming Missions, SSC18-WKIX-01 https://digitalcommons.usu.edu/smallsat/2018/all2018/471/
Zhu, H., Tian, W., Li, A., & Zhang, M. 2017, MNRAS, 471, 3494